A Burst-Mode Photon-Counting Receiver with Automatic Channel Estimation and Bit Rate Detection

Hemonth G. Rao, Catherine E. DeVoe, Andrew S. Fletcher, Igor D. Gaschits, Farhad Hakimi, Scott A. Hamilton, Nicholas D. Hardy, John G. Ingwersen, Richard D. Kaminsky, John D. Moores, Marvin S. Scheinbart, Timothy M. Yarnall

MIT Lincoln Laboratory, 244 Wood St., Lexington, MA USA 02421

ABSTRACT

We demonstrate a multi-rate burst-mode photon-counting receiver for undersea communication at data rates up to 10.416 Mb/s over a 30-foot water channel. To the best of our knowledge, this is the first demonstration of burst-mode photon-counting communication. With added attenuation, the maximum link loss is 97.1 dB at λ=517 nm. In clear ocean water, this equates to link distances up to 148 meters. For λ=470 nm, the achievable link distance in clear ocean water is 450 meters. The receiver incorporates soft-decision forward error correction (FEC) based on a product code of an inner LDPC code and an outer BCH code. The FEC supports multiple code rates to achieve error-free performance. We have selected a burst-mode receiver architecture to provide robust performance with respect to unpredictable channel obstructions. The receiver is capable of on-the-fly data rate detection and adapts to changing levels of signal and background light. The receiver updates its phase alignment and channel estimates every 1.6 ms, allowing for rapid changes in water quality as well as motion between transmitter and receiver. We demonstrate on-the-fly rate detection, channel BER within 0.2 dB of theory across all data rates, and error-free performance within 1.82 dB of soft-decision capacity across all tested code rates. All signal processing is done in FPGAs and runs continuously in real time.

Keywords: optical communications, photon counting, burst-mode receivers, underwater communications, soft-decision

1. INTRODUCTION

Underwater wireless optical communication promises to increase data rates beyond those practically achievable using acoustics, with link lengths potentially extending to hundreds of meters[1,2]. Several recent optical experiments have demonstrated rates in the range of megabits to gigabits per second[3-7]. Compared to atmospheric or space-based wireless optical communication, underwater communication faces unique challenges. The absorption spectrum of water dictates that the communication wavelength should be blue or green[1], rather than the infrared wavelengths used in air/space links[8,9]. Scattering over short distances transfers significant energy outside the beam's diffraction-limited divergence profile[5], which limits the usefulness of single-mode fiber components at the receiver. Together, these conditions argue against some of the key technologies (e.g., erbium-doped fiber amplifiers or EDFAs) used to enable high data rates in air or space wireless optical links.

Water quality can significantly impact performance. Whereas diffraction-limited air/space links experience attenuation primarily as the inverse-square of distance, loss due to water absorption and scattering is dominated by the Beer-Lambert law:

$$I(z) = I(0)e^{-cz} = I(0)e^{-(a+b)z} \tag{1}$$

where a and b represent absorption and scattering coefficients, respectively, c is the overall loss due to the both effects, and z is distance. Table 1 shows characteristic values for these coefficients for several water types. Because of the wide

variation in optical loss with water type and optical wavelength, it is useful to measure link distance in terms of extinction lengths[5], where an extinction length is c^{-1}.

Water Types	λ	a [m^{-1}]	b [m^{-1}]	c [m^{-1}]	EL	Source
Turbid Harbor	514 nm (green)	0.37	1.8	2.2	0.45 m	Petzold[10] (1972)
Clear Ocean	514 nm (green)	0.11	0.037	0.15	6.7 m	Petzold (1972)
	470 nm (blue)	0.038*	0.012*	0.05	20 m	Pontbriand[11] (2008)

*Assumed same ratio of b/c as Petzold's clear ocean case.

Table 1: Absorption, scattering, and loss for various water type at different wavelengths. Parameters: a = absorption, b = scattering, $c = a+b$, EL = extinction length = c^{-1}.

Scattering at any given location is subject to seasonal variation as suspended biological matter becomes more or less prevalent. Furthermore, scattered sunlight contributes to background noise. Therefore, background noise is subject to variations in water quality, available sunlight at depth, receiver pointing angle, overhead clouds, and time of day.

As can be seen from Table 1, signal attenuation over a realistic 10 meter green-light link could vary between 6.6 dB (clear ocean) and 96 dB (turbid harbor). Similarly large variations in link loss can occur for a particular water type if the distance between communicating terminals is changing. Faster changes that could result in deep signal losses (i.e., fades) can be caused by bubbles, turbulence, or large agents such as fish that appear in the path of the signal. To the best of our knowledge, there are currently no general models to predict the appearance or duration of all of these causes of fading.

2. SYSTEM CONSIDERATIONS

Due to variability in the water channel, a robust optical link must be designed against quasi-static link losses ranging from almost nothing to roughly 100 dB. Similarly, the link must be able to tolerate and adapt to a range of background light levels. The link can be designed to vary its data rate according to changes in link quality, allowing high data rates in the presence of low loss and low background, and robust communications in the presence of low light or high noise. While linear detectors including avalanche photodetectors (APDs) have achieved multi-gigabit per second rates, their sensitivity is typically limited by thermal noise. On the other hand, photon-counting detectors can achieve very high sensitivities, albeit in most cases limited to more moderate data rates.

Detector sensitivity

For reasons of environmental safety and to reduce size and complexity, we have limited our consideration of transmitter output power to a range of 10 mW to 100 mW. Therefore, referring to the 10-meter turbid harbor case and neglecting beam spreading loss, -85 dBm to -75 dBm can be available at the receiver. Again, given the nature of the beam at the receiver and the current state of the art, we assume direct detection without the benefit of optical pre-amplification. We are currently investigating the use of photon-counting detectors for signals near the minimum expected signal level and linear APDs for higher data rates and higher signal powers. The combination of both detectors is expected to allow operation over the full dynamic range. The remainder of this paper will focus on the photon-counting receiver. In this case, as for linear APDs, a desirable figure of merit for efficient rate fallback is near-theoretical performance in terms of required photons per bit for a given modulation format and for a given bit error rate (BER).

Photon-counting links have been demonstrated with pulse-position modulation (PPM) to achieve high sensitivity[12,13]. When coupled with an average-power limited transmit optical amplifier, near-theoretical rate fallback can be achieved by increasing the size M of the symbol alphabet[14] or by inserting empty space between symbols[15]. However, in the current system, we choose on-off keying (OOK) for our modulation. In this case, rate fallback occurs by lengthening the symbol duration.

Forward error correction

End-to-end performance can be improved through the use of forward error correction (FEC), allowing less received power for the same target BER. Since we are interested in loss-limited links, FEC is a key enabling technology. Older codes such as Reed-Solomon have a relatively small footprint and high throughput. However, newer soft-decision codes based on low-density parity check codes (LDPCs) can provide performance near capacity[16]. The input to a soft-decision FEC is a vector of log likelihood ratios (LLRs), where each LLR represents an estimate of a transmitted bit. For a given received signal r_i corresponding to a transmitted bit x_i, its LLR is

$$\text{LLR} = \ln \frac{p(x_i=1 \,|r_i)}{p(x_i=0 \,|r_i)} \tag{2}$$

Some soft-decision FECs available today allow run-time configuration of their code rate, or the fraction of transmitted bits that correspond to user data (with the remainder consisting of parity bits). Code rate can be used as an additional parameter to trade robustness vs. data rate.

For the data rates of interest in this paper, the expense of a soft decision FEC is justifiable, given recently-available dense programmable logic. However, in order to employ it successfully, the receiver must be able to estimate the channel's signal and noise characteristics in order to compute the LLRs.

Synchronization

Symbol synchronization is a driving requirement in this design. As already mentioned, the frequency and duration of channel disturbances is currently unknown. We pessimistically assume that any disturbance can cause a complete loss of signal and may last for an extended period of time. It is not unreasonable to expect channel disturbances that cause outages lasting several seconds. Furthermore, it may be desirable to establish and tear down links quickly in order to save power, reduce light pollution, or address multiple communication partners quickly. A receiver capable of communicating in such an environment is fundamentally designed for *burst-mode* operation[17].

Clock sources are a fundamental component of any communication system. It is a design goal in this paper to accept the clock stability of the "best of breed" among widely-available commercial clock oscillators. Such components tend to be available from multiple vendors, have small physical footprints, low power requirements, and fast start-up times. On the other hand, oscillators with higher stability may be obtainable, but from fewer vendors. They may also require thermal or other controls that are expensive, bulky, and slow to initialize. Since space in an underwater terminal may be extremely limited, it is important to design the burst-mode waveform to work with the realistic specifications of a small, low-power oscillator.

Channel Rate and Code Rate Negotiation

It is desirable to support dynamic changes in data rate and code rate in accordance with changes in link conditions. If these changes must be pre-announced between transmitter and receiver, changes can either be negotiated within the optical channel using an in-band control channel, or else a more-reliable side-channel can be used to negotiate the change. In-band negotiation is problematic. If the information rate needs to be reduced because of link impairments, it implies that the link is not reliable enough for the in-band channel to negotiate the change. Out-of-band negotiation using a side channel is also unattractive. In the underwater environment, the most obvious candidate for out-of-band communication is an acoustic channel[1]. However, the acoustic link requires extra hardware. Furthermore, the acoustic signal is much less spatially confined than the optical signal. This spreading is undesirable from an environmental perspective.

Proposed solution

In this paper, we propose and demonstrate a burst-mode photon-counting receiver that automatically determines channel rate and FEC code rate without the need for negotiation with the transmitter. The receiver's synchronization system provides periodic updates of the incoming data's estimated clock phase, as well as estimates of the signal and background light levels. Light level estimates are used to generate soft-decision information on a bit-by-bit basis for use by the receiver's forward error correction system.

3. SYSTEM DESCRIPTION

Experimental hardware

Figure 1 shows the experimental setup used to demonstrate communication. The experiment is a uni-directional link consisting of a transmitter, 30-foot pipe filled with water, and a receiver.
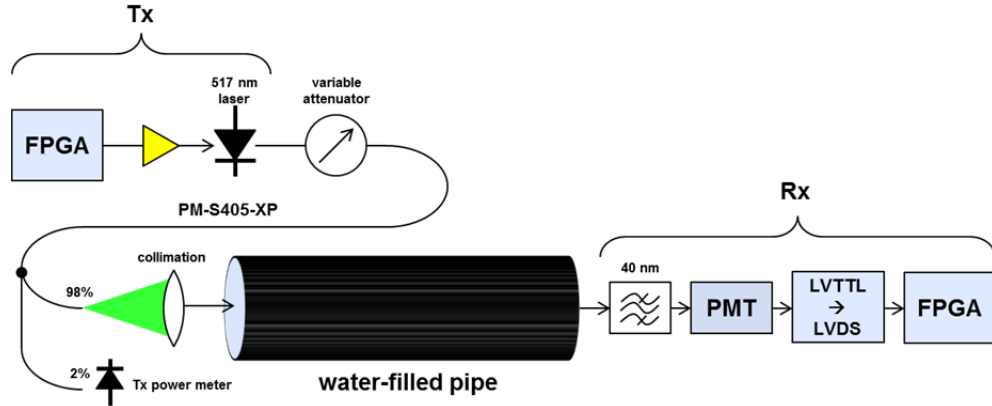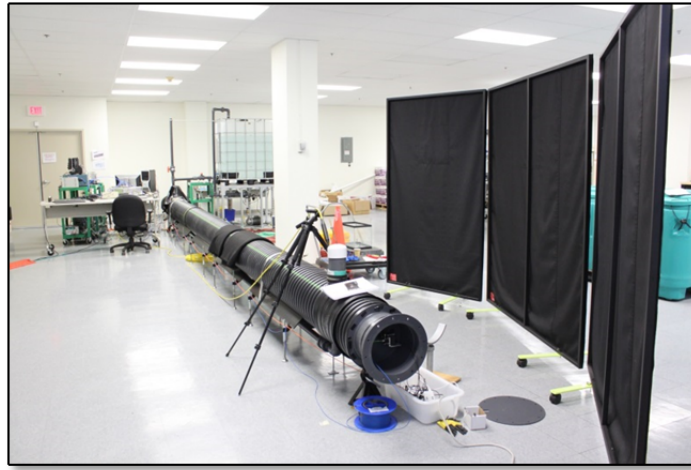

Figure 1. Experimental testbed.

Figure 2: 30-foot water pipe testbed.

Figure 2 shows the water pipe testbed. The transmitter end is in the foreground, and the receiver end is in the back. The pipe can be filled with water, emptied into a reservoir (shown in the back of the picture), and cleaned of biological agents with UV light. If desired, controlled scattering agents can be added to the pipe. The pipe itself is opaque at the transmitter's wavelength and is sealed at both ends to keep out stray light.

In this experiment, the pipe is filled with filtered tap water. The optical loss through the pipe is 8 dB. Additional loss is introduced via an optical attenuator.

The transmitter consists of a Xilinx Virtex 7 field-programmable gate array (FPGA) board driving a directly-modulated laser through an RF amplifier. The laser's wavelength is 517 nm with an approximate 1 nm bandwidth. It supports an output power of 100 mW and modulation up to 250 MHz. It provides extinction greater than 30 dB. The laser's output is fiber- coupled. The output is attenuated before proceeding through 10 meters of Nufern polarization-maintaining PM-S405-XP fiber (Figure 2a). Most of this fiber's output is collimated and launched into the water pipe. Two percent of the fiber output is read with a power meter to determine power at the launch end. After coupling losses, the launch power into the water pipe is 13 dBm.

The receiver comprises a 40 nm dichroic optical filter, a Hamamatsu H10682-210 photomultiplier tube (PMT) and a Xilinx Virtex 7 FPGA board containing a single XC7VX485T FPGA. The PMT is a single-element detector operated at room temperature that has a measured quantum efficiency of 0.1274, a maximum dark count rate of 100 s^{-1}, an output pulse width of 8 ns, and a dead time of 20 ns. For CW input light, its output is very linear with input power up to approximately 3 Mcounts/s; for higher input powers, the count rate deviates until it saturates at approximately 18.3 Mcounts/s (see Figure 3a).
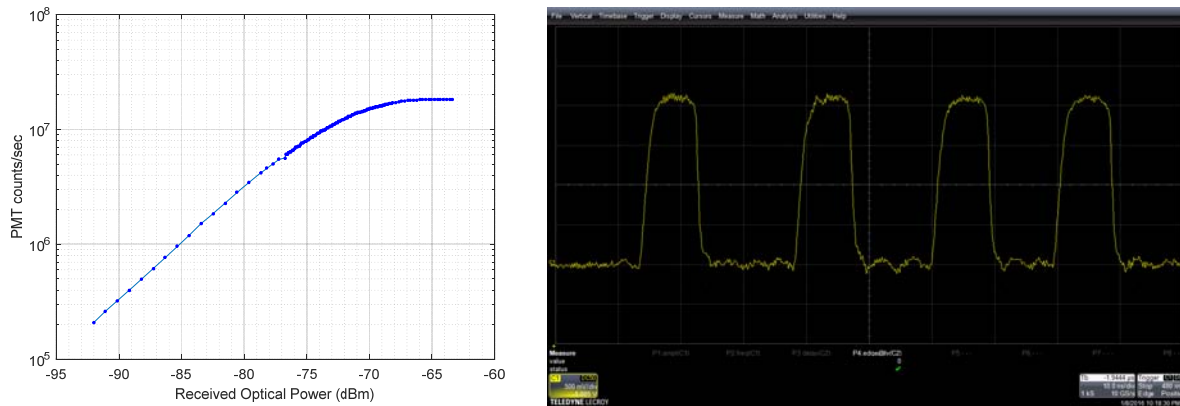

Figure 3. a) PMT count linearity vs. input power. b) Output for high input power

Figure 3b shows an example of the PMT output for high input power. The last two pulses show both the pulse width and blocking time. The output of the PMT is dc-coupled low-voltage TTL. We convert the output to low-voltage differential signaling (LVDS) in order to interface to the FPGA. The FPGA samples the PMT output at 500 Msamples/s.

Transmitted waveform

Since the system is limited by the bandwidth of the single-element PMT, we selected OOK modulation. It is well-known that non-return to zero (NRZ) OOK does not have a clock frequency component, which complicates receiver synchronization. Previous demonstrations have employed periodic training sequences embedded in the transmitted signal in order to achieve synchronization[17]. We opt instead for a high duty-cycle return-to-zero (RZ) format, which does have a clock frequency component. Figure 4 shows that RZ pulse used here has a duty cycle of 11/12.
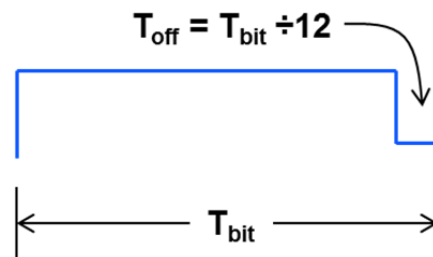

Figure 4. High duty cycle RZ-OOK pulse

The transmitter can select between data rates of 1.302 Mb/s, 5.208 Mb/s, and 10.416 Mb/s. The RZ duty cycle is the same in all cases. It can be seen that in the lowest data rate, the off time during each pulse exceeds the dead time of the PMT. In the case of the higher two data rates, the off time is 16 ns and 8 ns respectively, whereas the dead time is 20 ns. Therefore, neglecting dark counts, the off time of the lowest rate guarantees that the PMT is armed at the beginning of each pulse, and at the higher data rates the off time significantly improves the chance that the PMT is armed.

The transmitted data is organized into frames, as shown in Figure 5. Some frame fields are unused and reserved for future development. The 96-bit Frame Alignment Sequence (FAS) at the beginning of the frame is a fixed pattern used to delimit the start of each frame. Each frame is numbered at the transmitter with a Frame Sequence Number (FSN), which is encoded into a 127-bit BCH(127,22) codeword[19], padded to 128 bits, and repeated three times within the frame. At the receiver, the three copies are combined into one by performing a bit-by-bit vote, otherwise known as triple-mode

redundancy (TMR). TMR improves robustness by ensuring that the FSN can be decoded at higher BER than the payload.
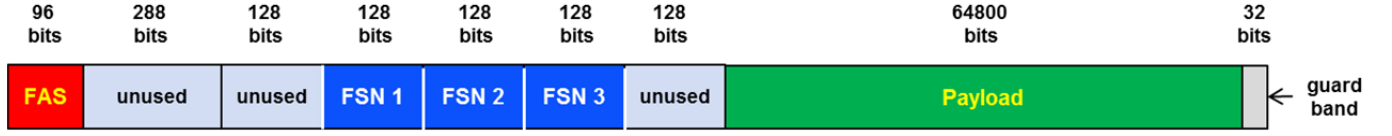

96 bits	288 bits	128 bits	128 bits	128 bits	128 bits	128 bits	64800 bits	32 bits
FAS	unused	unused	FSN 1	FSN 2	FSN 3	unused	Payload	← guard band

Figure 5. Frame structure

The payload is a $2^{16}-1$ pseudo-random bit stream (PRBS) encoded using an LDPC+BCH product code. The PRBS sequence restarts with each frame. The FEC codec implementation used here was developed at MIT Lincoln Laboratory. The codec runs in real time on the FPGA. The decoder accepts a soft-decision input with 6-bit quantization of LLRs. It supports a wide range of code rates (1/4, 1/3, 2/5, 1/2, 3/5, 2/3, 3/4, 5/6, 8/9, and 9/10) that can be selected and changed during run-time.

The end of the frame consists of 32 bits of a fixed pattern used to allow a gap between successive frames. Since we assume burst-mode transmission, we assume that the receiver clock phase is nearly constant with respect to the transmitter over the duration of one frame. However, because we assume moderate-stability clocks, the receiver clock phase is allowed to drift slowly with respect to the transmitter. The inter-frame gap of 32 bits is much larger than required to allow clock slips between frames, but it is a convenient size for our transmitter implementation.

Receiver functions

The receiver determines the data rate; estimates signal and background light levels; performs data clock alignment, demodulation, and LLR generation; and processes frame data continuously in real time. Figure 6 shows a block diagram of the FPGA code responsible for performing these functions.

An individual PMT output pulse's duration is significantly longer than the FPGA's sampling period. Therefore, the FPGA registers PMT events as the rising edges of the PMT output. The derived edges are buffered in a delay FIFO for 1.572864 ms and are also fed to three alignment blocks. Each alignment block corresponds to a supported channel data rate. As will be described later, each alignment block assumes a given channel rate. The alignment block for the dth channel rate derives an estimate $\varphi^{(d)}$ for a bit phase delay between the incoming stream and the receiver's own bit clock. It also estimates $n_0^{(d)}$ and $n_1^{(d)}$, which are the average number of background and signal photons per bit, respectively, for the dth data rate. The alignment blocks are therefore also responsible for channel estimation. All three alignment blocks are synchronized to start estimating at the same time, to report estimates together every 1.572864 ns, and immediately start the next estimate. Thus, timing recovery can be viewed as an "integrate-and-dump" event occurring with a strict periodicity.
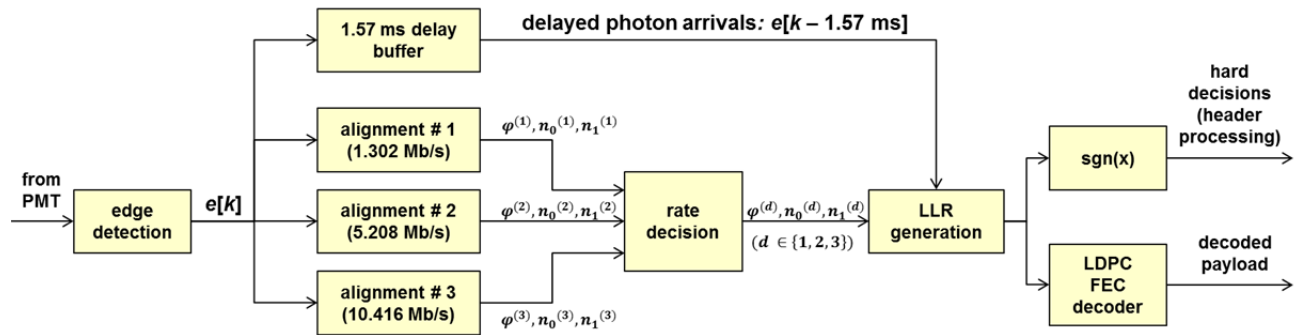

Figure 6. Receiver FPGA block diagram. $e[k]$ = sampled time series of photon arrivals; $\varphi^{(d)}$ = bit phase for d^{th} data rate; $n_0^{(d)}$ = average number of photons in a "0" bit and $n_1^{(d)}$ = average number of photons in a "1" bit for the dth data rate.

Receiver alignment and channel estimation

Because the FPGA samples the PMT output at a rate of 500 MHz, at any data rate each bit is oversampled N times. Each alignment block maintains N counters, one for each possible bit phase. The "off" time in the transmitted pulses (Figure 4) provides a periodic structure that can be used for timing alignment. Each counter accumulates detected

photon events that fall into the "off" time for the RZ bit at that phase. The counters accumulate events for the equivalent of M bits, which is again dependent on the data rate for that alignment block. Table 2 shows the oversampling N and integration time M for each data rate. As can be seen, the integration time $NM \cdot 2$ ns is a constant 1.572864 ms.

Channel Rate (Mb/s)	N = Oversampling	M = Integration Time (bits)
1.302	384	2048
5.208	96	8192
10.416	48	16384

Table 2. Alignment parameters.

Figure 7 shows the operation of the integration counters for a given data rate. A dark count in the "off" time of the second bit is shown. Any counters whose "off" window overlaps with a detected photon event will accumulate it. Assuming that $n_0 < n_1$, the best-matching phase will correspond to the counter with the minimum value after M bits of integration.
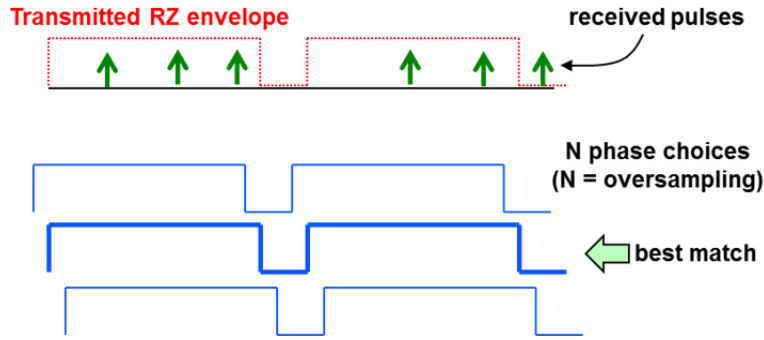

Figure 7. Integration of PMT counts within one alignment block

The frame length shown (minus the guard band) shown in Figure 5 and the oversampling parameter N in Table 2 determine the minimum stability required from the receiver's clock oscillator with respect to the transmitter's oscillator. In the worst case where $N=384$, allowing for a fast transmitter and a slow receiver (or vice versa), and allowing only 1 ns (i.e., half a sample period) of timing slip between transmitter and receiver over the duration of one frame, then an individual oscillator must have a stability of 10 parts per billion. Fortunately, oscillators of this class are readily available from multiple vendors at low cost, having small size and fast initialization times.

Demodulation and subsequent processing

The receiver decides on the incoming data rate depending on which alignment block reports the highest value of the ratio n_1/n_0. The selected estimate for φ is used to align the delayed edge data to the receiver's own bit clock, while n_0 and n_1 are used to generate LLRs from the PMT rising edges. Assuming that the PMT rising edges are Poisson-distributed, the LLR for a given bit with n detected photons can be calculated as

$$\text{LLR} = \ln \frac{p(1|n)}{p(0|n)} = \ln \frac{p(n|1)}{p(n|0)} = \ln \frac{e^{-n_1} \cdot n_1{}^n}{e^{-n_0} \cdot n_0{}^n} = n_0 - n_1 + n \cdot \left(\ln n_1 - \ln n_0 \right) \tag{3}$$

The delay FIFO allows the PMT data to generate estimates for φ, n_0, and n_1 and then be processed with those same estimates. With the FIFO, the channel delay, signal, and background light levels need only be quasi-static over approximately 1.6 ms; without the FIFO, the channel would need to be stable for twice as long. Fortunately, the FIFO could be implemented using only a small amount of FPGA block RAMs (BRAMs). No external memory was required.

The sign of the LLR is used to generate hard decisions. For a given bit with an LLR ≥ 0, the corresponding hard decision is a "1". Otherwise, the hard decision is a "0". This implies an effective hard-decision threshold of

$$n_{th} = \frac{n_1 - n_0}{\ln n_1 - \ln n_0} \tag{4}$$

Hard decisions are used to process only the FAS and FSN fields of the frame.

Frame synchronization occurs when the FAS is captured with a BER less than 0.167 across the 96-bit field. Because we assume burst-mode synchronization, frame synchronization lasts for one frame only. At the end of each frame, the receiver again begins searching for the FAS.

As mentioned earlier, the receiver uses all three copies of the BCH-encoded FSN (Figure 5). A bit-by-bit vote among the three copies provides a more reliable version of the BCH codeword prior to decoding. The decoded FSN is used by higher-layer reliability mechanisms to track individual frames.

4. RESULTS

Figure 9 shows measured n_0, n_1, and the resulting n_{th} at 10.416 Mb/s as a function of input optical power. It can be seen that the background light level rises with the signal level with nearly constant proportionality below -77 dBm. In this input power range, the ratio between the two is approximately 27 dB. This is similar to the stated transmitter extinction, indicating that background levels in this experiment are dominated by transmitter extinction. The effective extinction seen at the receiver, n_1 / n_0, can be affected slightly by PMT saturation, since it affects n_1 and n_0 differently.
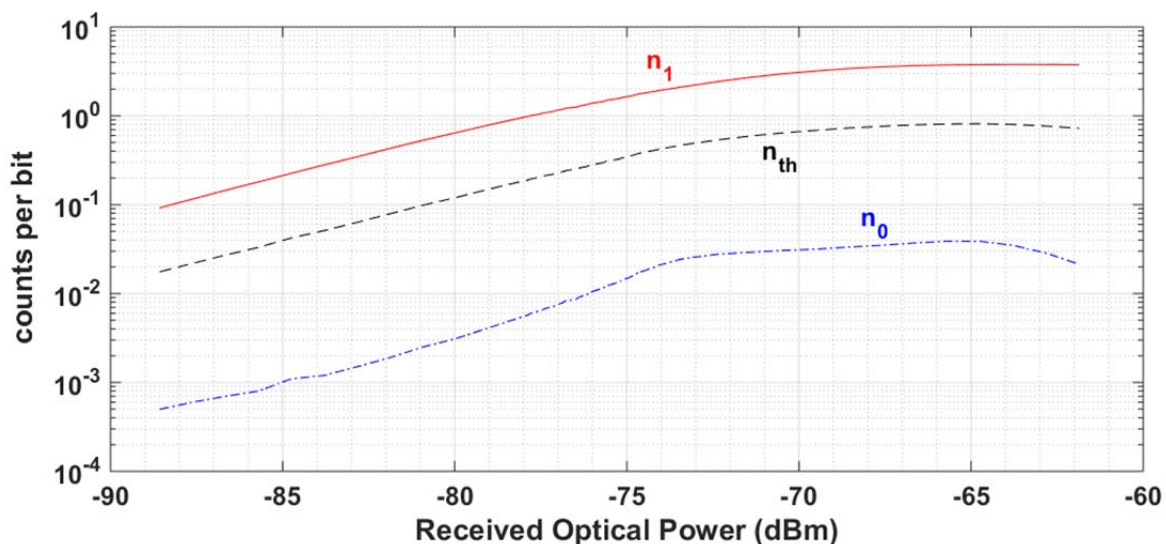

Figure 9. Measured n_0, n_1, and n_{th} at 10.416 Mb/s vs. received optical power.

At very high input powers, measured n_0 decreases with received power. This behavior becomes more pronounced with increasing data rate. In that case, the "off" time of each pulse is comparable to or less than the blocking time. High input powers increase the probability of a detected photon at the end of the "on" part of a "1" bit, blocking detection of photons in the "off" part of the bit. Saturation is less pronounced at the lower data rates, since in those cases less transmitted power is required. At the lowest data rate (1.302 Mb/s), saturation effects are absent over all input powers of interest.

Figure 9 also shows that for 10.416 Mb/s, n_{th} rises with input power, but it never crosses 1. In this case, the rise of n_{th} is limited by the PMT's saturation. However, for the other data rates, n_{th} can assume positive integer values with sufficient input power.

Figure 10 shows the measured hard-decision BER as a function of input power and data rate. Whenever data rate was changed, it was done without warning the receiver. In all cases, the receiver quickly and successfully re-acquired the signal, which validates receiver's automatic rate detection design. The FEC decoder is able to produce error-free output for half-rate encoded input when the hard-decision BER is approximately 7×10^{-2}.
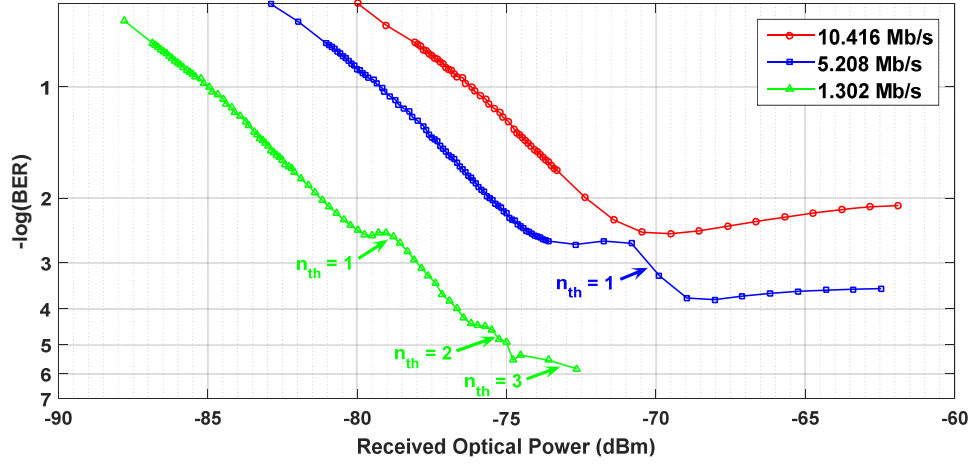
Figure 10. Measured hard-decision BER vs. input power. Also shown: for each data rate, locations where n_{th} takes a positive integral value.

The BER monotonically drops in all cases until the input power increases sufficiently. Beyond a certain point, the BER exhibits a series of step-like changes. Figure 11 shows that a gradual rise in the total BER occurs when the BER is dominated by "0" → "1" errors, rather than "1" → "0" errors. The rise is mitigated when the effective threshold n_{th} reaches an integral value. When PMT saturates, n_{th} cannot reach the next integral value and the BER exhibits an error floor. Saturation could be seen for 10.416 Mb/s and 5.208 Mb/s at higher powers.
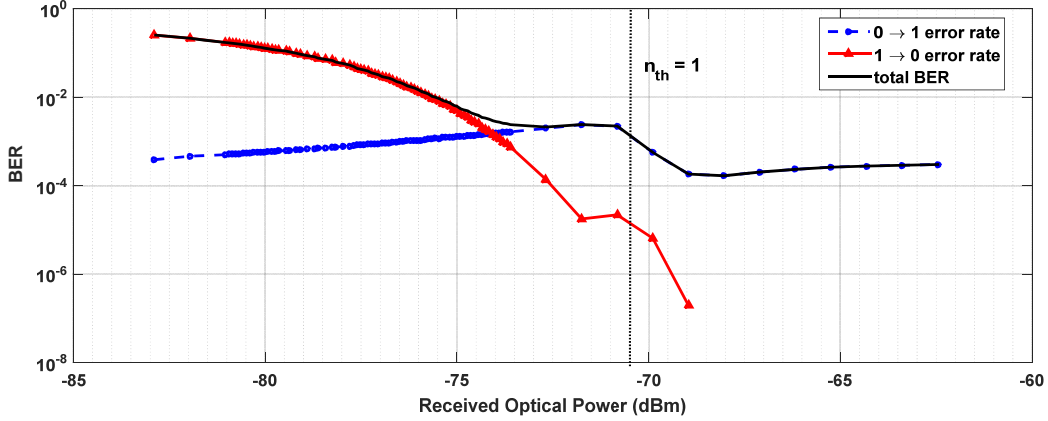

Figure 11. Measured "0" → "1" BER and "1" → "0" BER for 5.208 Mb/s near $n_{th} = 1$.

The performance across data rates can be compared by normalizing the input power to detected photons per bit (obtained with the measured quantum efficiency of 0.1274). Figure 12 shows the measured hard-decision BER and post-FEC BER for all data rates where the FEC code rate is 0.5. Also shown is the expected BER according to theory:

$$BER_{theory} = \frac{1}{2} e^{-n_1} \qquad (5)$$

This model assumes background light (i.e., n_0) is negligible. The channel BER at each rate agrees well with theory up to 3.5 dB photons per bit. The implementation penalty for 10.416 Mb/s and 5.208 Mb/s is ≤ 0.1 dB, while the penalty for 1.302 Mb/s is 0.2 dB. Beyond 3.5 dB photons per bit, the simple model of Equation (5) is inadequate to explain effects due to PMT saturation and effective-threshold changes due to non-negligible n_0. Fortunately, the FEC codec produces error-free output below 1 photon per bit, well before these effects take hold. The post-FEC BER vs. detected photons per bit is nearly identical between 10.416 Mb/s and 5.208 Mb/s. The increased penalty seen for 1.302 Mb/s channel BER translates to a 0.2 dB penalty for its post-FEC performance.

Figure 12 shows that the receiver achieves near-constant efficiency in terms of BER performance vs. photons per bit across data rates, indicating that rate fallback can be achieved without additional penalty. The post-FEC BER for code rate = ½ is also shown. The post-FEC BER falls off very rapidly as the input power approaches 0.5 dB photons per bit. Beyond this point, the post-FEC BER was measured to be 0 after integrating for one hour. It is evident from Figure 10 and Figure 12 that strong FEC capable of operating in the low-light regime can achieve error-free communication even if the channel BER shows an error floor above 10^{-3} due to PMT saturation.
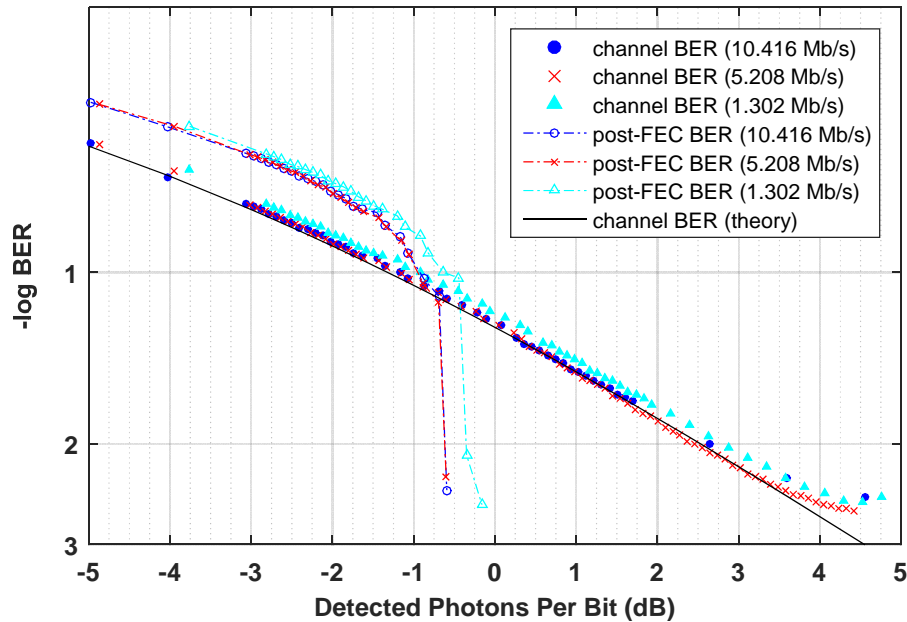

Figure 12. Measured hard-decision and post-FEC (code rate = 1/2) BER across all data rates, normalized to detected photons per bit.
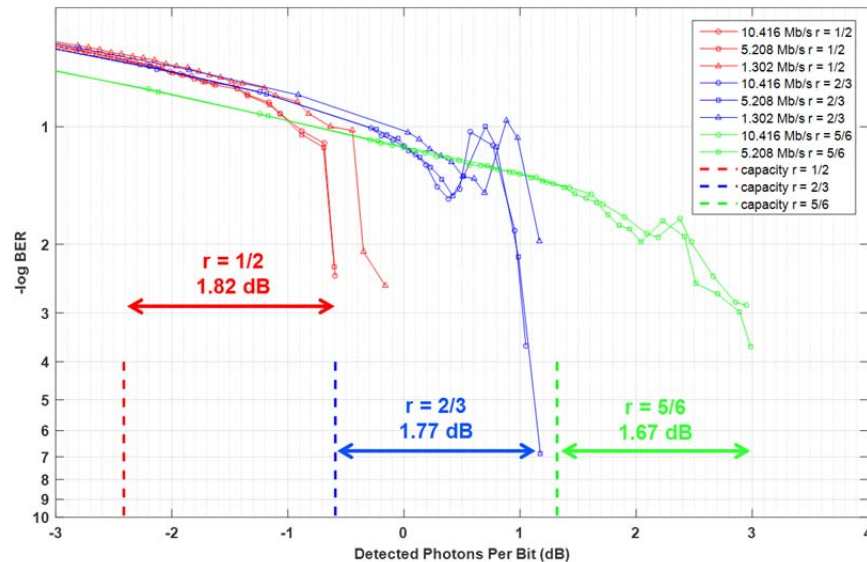

Figure 13. Distance to capacity vs. code rate (rate r = 1/2, 2/3, and 5/6). Shown: post-FEC BERs for several channel rates and code rates.

Figure 13 shows the distance between measured FEC performance and soft-decision capacity for various code rates. The plot shows multiple channel data rates. Again, the performance of 10.416 Mb/s and 5.208 Mb/s is nearly identical with respect to required photons per bit, while a 0.2 dB penalty is seen for 1.302 Mb/s. Since the increased penalty for 1.302 Mb/s is believed to be caused by the hardware implementation, the distance to capacity was measured against the other data rates. The gap was found to be 1.67 – 1.82 dB, decreasing with increasing code rate.

5. DISCUSSION

For the data rates presented here, it is not expected that scattering-induced pulse dispersion will introduce significant penalties. Rather, as Equation (1) indicates, scattering can be grouped along with absorption as a loss mechanism. In this sense, the external optical attenuation used in this experiment combines with the loss in the water pipe. After coupling losses, the transmitter's average power at launch is 13 dBm. Given the sensitivities of the receiver for the presented data rates and ½-rate FEC, this allows for a maximum link loss of 88.3 dB for 10.416 Mb/s to 97.1 dB for 1.302 Mb/s. For a green-wavelength link in clear ocean water, this equates to link distances up to 148 meters. For blue-wavelength links, the PMT's quantum efficiency increases. It is expected that the improved quantum efficiency would allow a maximum link loss of 98.4 dB. Furthermore, as Table 1 indicates, propagation losses should be lower for $\lambda =$ 470 nm. When both effects are considered, it is expected that a blue-wavelength link in clear ocean water should be capable of distances up to 450 meters.

6. CONCLUSION

This paper presented the motivation for developing a novel high-sensitivity, burst-mode, multi-rate, photon-counting receiver for underwater optical communication. It is expected that wide variability in water conditions (both from location to location and over time in a single location) will require high dynamic range, for which photon counting can be a key component. The burst-mode nature of the demonstrated receiver allows for a small-sized implementation that can handle channel outages of unpredictable duration. This burst-mode receiver also detects the incoming data rate automatically, removing the need for a reliable out-of-band management link. The receiver estimates the channel conditions every 1.6 ms, adapting to changes in signal strength and background light. The receiver achieves near-theoretical performance (< 0.2 dB penalty) across 1.302 Mb/s, 5.208 Mb/s, and 10.416 Mb/s. The receiver includes LDPC-based, soft-decision forward error correction to provide error-free communication when the channel BER is as high as $7x10^{-2}$. This allows robust transmission at rates suitable for several applications, including compressed high-definition video, while allowing for efficient rate fallback across 12.5 dB (i.e., almost three extinction lengths) of dynamic range.

ACKNOWLEDGEMENTS

REFERENCES

[1] Farr, N., Bowen, A., Ware, J., and Pontbriand, C., "An integrated, underwater optical/acoustic communications system," OCEANS 2010, 24-27 May 2010.
[2] Arnon, S. and Kedar, D., "Non-line-of-sight underwater optical wireless communication network," *J. Opt. Soc. Am. A*, v. 26 no. 3 (2009).
[3] Cochenour, B., Mullen, L., and Laux, A., "Phase coherent digital communications for wireless optical links in turbid underwater environments," OCEANS 2007, 29 September – 4 October 2007.
[4] Brundage, H., "Designing a wireless underwater optical communication system," Master's thesis, Massachusetts Institute of Technology (2010).
[5] Snow, J.B., Flatley, J.P., Freeman, D.E., Landry, M.A., Lindstrom, C.E., Longacre., J.R., and Schwartz, J.A., "Underwater propagation of high data rate laser communication pulses," Proc. SPIE 1750, 419-427 (1992).
[6] Hanson, F. and Radic, S., "High bandwidth underwater optical communication," *Applied Optics*, v. 47 no. 2 (2008).

[7] Oubei., H.M., Duran, J.R., Janjua, B., Wang, H.-Y., Tsai, C.-T., Chi, Y.-C., Ng, T.K., Kuo, H.-C., He, J.-H., Alouini, M.-S., Lin, G.-R., and Ooi, B.S., "4.8 Gb/s 16-QAM-OFDM transmission based on compact 450-nm laser for underwater wireless optical communication," *Optics Express*, v. 23 no. 18 (2015).

[8] Krainak, M., Unger, G., and Sun, X., "High-sensitivity 1064-nm 50-Mbps direct-detection free-space communications receiver," CLEO 1992, paper CThI16 (1992).

[9] Boroson, D.M., Scozzafava, J.J., Murphy, D.V., Robinson, B.S., and Shaw, H., "The Lunar Laser Communications Demonstration (LLCD)," SMC-IT 2009 19-23 July 2009 23-28 (2009).

[10] Petzold, T.J., "Volume scattering functions for selected ocean waters," Scripps Institute of Oceanography SIO 72-78 (1972)

[11] Pontbriand, C., Farr, N., Ware, J., Preisig, J., Popenoe, H., "Diffuse high-bandwidth optical communications," OCEANS 2008, 15-18 September 2008.

[12] Grein, M.E., Elgin, L.E., Robinson, B.S., Kachelmyer, A.L., Caplan, D.O., Stevens, M.L., Carney, J.J., Hamilton, S.A., and Boroson, D.M., "Demonstration of a 1550-nm Photon-Counting Receiver with < 0.5 Detected Photon-Per-Bit Sensitivity at 187.5 Mb/s," CLEO/QELS 2008, paper CWN5 (2008).

[13] Robinson, B.S., Kerman, A.J., Dauler, E.A., Barron, R.J., Caplan, D.O., Stevens, M.L., Carney, J.J., Hamilton, S.A., Yang, J.K.W., and Berggren, K.K., "781 Mbit/s photon-counting optical communications using a superconducting nanowire detector," *Optics Letters*, v. 31 no. 4 444-446 (2006).

[14] Caplan, D.O., Robinson, B.S., Murphy, R.J., and Stevens, M.L., "Demonstration of 2.5-Gslot/s optically-preamplified M-PPM with 4 photons/bit receiver sensitivity," OFC/NFOEC 2005 paper PDP32 (2005).

[15] Spellmeyer, N.W., Bernstein, S.L., Boroson, D.M., Caplan, D.O., Fletcher, A.S., Hamilton, S.A., Murphy, R.J., Norvig, M., Rao, H.G., Robinson, B.S., Savage, S.J., Schulein, R.T., Stevens, M.L., and Wang, J.P., "Demonstration of a multi-rate thresholded preamplified 16-ary pulse-position-modulation," OFC/NFOEC 2010 paper OThT5 (2010).

[16] MacKay, D.J.C., "Good error-correcting codes based on very sparse matrices," *IEEE Transactions on Information Theory*, vol. 45 no. 2 (1999).

[17] Mendinueta, J.D.M., Mitchell, J.E., Bayvel, P., and Thomsen, B.C., "Digital dual-rate burst-mode receiver for 10G and 1G coexistence in optical access networks," *Optics Express* v. 19 no. 15 14060-14066 (2011).

[18] Hiskett, P.A. and Lamb, R.A., "Underwater optical communications with a single photon-counting system," Proc. SPIE 9114, 1-15 (2014).

[19] Lin, S., and Costello, D.J. *Error Control Coding: Fundamentals and Applications*. 2nd Ed. Pearson Prentice Hall (Upper Saddle River, NJ). 2004.